# Evolution of Defect Structures and Deep Subgap States during Annealing of Amorphous In-Ga-Zn Oxide for Thin-Film Transistors

Junjun Jia, Ayaka Suko, and Yuzo Shigesato*
*Graduate School of Science and Engineering, Aoyama Gakuin University, 5-10-1 Fuchinobe, Chuo, Sagamihara 252-5258, Japan*

Toshihiro Okajima
*Kyushu Synchrotron Light Research Center, 8-7 Yayoigaoka, Tosu, Saga 841-0005, Japan*

Keiko Inoue and Hiroyuki Hosomi
*Toray Research Center, Inc., Sonoyama 3-3-7, Otsu, Shiga 520-8567, Japan*

(Received 30 March 2017; revised manuscript received 18 November 2017; published 17 January 2018)

We investigate the evolution behavior of defect structures and the subgap states in In-Ga-Zn oxide (IGZO) films with increasing postannealing temperature by means of extended x-ray absorption fine-structure (EXAFS) measurements, positron annihilation lifetime spectroscopy (PALS), and cathodoluminescence (CL) spectroscopy, aiming to understand the relationship between defect structures and subgap states. EXAFS measurements reveal the varied oxygen coordination numbers around cations during postannealing and confirm two types of point defects, namely, excess oxygen around Ga atoms and oxygen deficiency around In and/or Zn atoms. PALS suggests the existence of cation-vacancy ($V_M$)-related clusters with neutral or negative charge in both amorphous and polycrystalline IGZO films. CL spectra show a main emission band at approximately 1.85 eV for IGZO films, and a distinct shoulder located at about 2.15 eV for IGZO films postannealed above 600 °C. These two emission bands are assigned to a recombination between the electrons in the conduction band and/or in the shallow donor levels near the conduction band and the acceptors trapped above the valence-band maximum. The shallow donors are attributed to the oxygen deficiency, and the acceptors are thought to possibly arise from the excess oxygen or the $V_M$-related clusters. These results open up an alternative route for understanding the device instability of amorphous IGZO-based thin-film transistors, especially the presence of the neutral or negatively charged $V_M$-related clusters in amorphous IGZO films.

DOI: 10.1103/PhysRevApplied.9.014018

## I. INTRODUCTION

Recently, amorphous oxide semiconductors have attracted considerable research interest as alternative materials for amorphous and polycrystalline Si-based thin-film transistors (TFTs) for use as channel materials in display applications and flexible electronic devices because of their high electron mobility, high transparency, and capability for low-temperature processing with excellent uniformity [1–5]. Among these materials, amorphous In-Ga-Zn oxide (IGZO) has attracted attention for use as a TFT active layer [2,5]. Amorphous IGZO TFTs have typical field-effect mobilities in the range of 10–20 $cm^2/V\,s$, which are obviously higher than those of amorphous Si TFTs; these high mobilities stem from their *s*-like conduction-band edges, which ensure robustness of *n*-type conductivity against disorders [2]. However, several studies have reported that amorphous IGZO TFTs exhibit environment-dependent instability, such as positive shifts of the threshold voltage under positive-bias stress (PBS) [6,7] and large negative shifts of threshold voltage under negative-bias illumination stress (NBIS) [8–11]. The origins of the PBS and NBIS instabilities remain controversial.

Oxygen-related defects, which originate from structural disorders in sputter-deposited amorphous IGZO films, have been considered to induce instability of amorphous IGZO TFTs [10,12]. The PBS instability has been attributed to electron traps, and the postdeposition thermal annealing (postannealing) has been reported to eliminate electron traps and mitigate device instability [13]. PBS is also sensitive to ambient gases such as $O_2$ and $H_2O$ [6], and to gate dielectric materials [14]. These observations suggest that PBS instability is caused by the adsorption of oxygen molecules from ambient atmosphere, or by electron traps in the gate dielectrics and/or the amorphous dielectric interface [6]. Moreover, PBS instability is observed in amorphous IGZO TFTs fabricated at high oxygen partial

*Corresponding author.
yuzo@chem.aoyama.ac.jp

 

pressures [7], and the oxygen interstitials created in bulk amorphous IGZO or at the interface have also been suggested as the origin of the electron trap for the PBS instability [15]. Furthermore, there remains the possibility of PBS instability from the undercoordinated cation pairs in the amorphous IGZO structure, as suggested by Han and Chang, where undercoordinated cation pairs (metal-metal bonding) with energies as low as 1.6 eV below the conduction-band minimum (CBM) can be formed through the capture of excess electrons, as predicted by theoretical calculations based on density-functional theory [16]. By contrast, the NBIS instability starts under illumination from a photon energy of approximately 2.3 eV and increasingly deteriorates with increases in the illumination intensity or energy [9,17]. It was suggested that the associated mechanism involves the generation of photoinduced holes owing to the existence of deep subgap states above the valence-band maximum (VBM) [17–20], which are associated with the density of states (DOS) above the VBM, as observed by the hard x-ray photoemission spectroscopy (HXPES) [21]. The microscopic origin of these deep subgap states remains unclear, including an explanation for the DOS above VBM observed through HXPES. NBIS instability is generally attributed to the varied oxygen coordination numbers (oxygen deficiency and interstitial oxygen) in the amorphous structure [22–26]. Kamiya and co-workers showed that the deep subgap states above the VBM can be explained by oxygen deficiency in the amorphous IGZO structure [23–25], and Körner *et al.* suggested that the deep subgap states above the VBM can be attributed to undercoordinated oxygen atoms [22], which is analogous to the concept of oxygen deficiency in the amorphous IGZO structure. Han *et al.* suggested that the oxygen interstitial defects act as electron traps near the VB tail in amorphous IGZO, and that they lead to a subsequent NBIS instability [26]. Both PBS and NBIS instabilities of amorphous IGZO TFTs are particularly associated with oxygen-related defects. However, the defect type and defect structure are still a subject of debate, and additional experimental evidence is needed to obtain a clear physical picture.

In practice, the postannealing at approximately 400 °C has been reported to be very effective for improving not only TFT performance but also stability and uniformity to overcome the instability issue of amorphous IGZO TFTs [27–30]; such treatment is considered to reduce the number of defect sites in the IGZO channel layers and/or interfaces. Tang *et al.* found that most subgap states are thermally unstable and decrease dramatically after postannealing at 400 °C in $O_2$ ambient [31]. Ide *et al.* reported that some deep subgap defects are eliminated by low-temperature postannealing in an $O_3$ ambient, even below 200 °C, and that postannealing at higher temperatures further improved device performance [27]. Such postannealing is considered to induce structural relaxation, including the relaxation of network configurations and the elimination of defects or voids [27,32], resulting in small subthreshold voltage swings and low operation voltages, and to mitigate the device instability of amorphous IGZO TFTs [23].

In this paper, our objective is to understand the correlation between defect structures and deep subgap states, and to reveal the microscopic origin of the deep subgap states, as well as the NIBS and/or PBS instabilities. We investigate the evolution behavior of defect structures and subgap states of the IGZO films during postannealing, examine the relationship between defect structures and subgap states from the viewpoint of evolution behavior, and identify the dominant factor affecting the NIBS or PBS instabilities. We use extended x-ray absorption fine-structure (EXAFS) measurements to determine the local structure of metal-oxygen bonds, and we apply positron annihilation lifetime spectroscopy (PALS) to examine the possible defect structures in as-grown and postannealed IGZO films. The changes in subgap states with increasing postannealing temperatures are investigated using cathodoluminescence (CL) spectroscopy.

## II. EXPERIMENTAL DETAILS

Amorphous IGZO films are deposited on unheated synthetic quartz glass substrates by means of direct-current (dc) magnetron sputtering with a 3-in.-diameter In-Ga-Zn oxide target ($In:Ga:Zn = 1:1:1$ in at. %, Toshima Manufacturing) at room temperature. The base pressure of the deposition chamber is less than $8.0 \times 10^{-4}$ Pa, and the working pressure is set to 0.5 Pa. The dc sputtering power is maintained at 50 W. The distance between the target and the substrate is 60 mm, and the maximum vertical magnetic-field strength at the magnetron target surface is 1000 G. Pure Ar gas (99.999%) is used as the sputtering gas. The $O_2$ flow ratio $[O_2/(Ar + O_2)]$ is set to 2% to deposit the as-grown film, which is the optimal condition for fabricating IGZO films with carrier densities lower than $10^{16}$ $cm^{-3}$ at room temperature; such conditions can yield good TFT performance [31,33]. In addition, amorphous IGZO films with different carrier densities are also deposited at an Ar flow of 100% (sample *A*), a $H_2$ flow ratio $[H_2/(Ar + H_2)]$ of 5% (sample *B*), and an $O_2$ flow ratio of 1% (sample *C*), as summarized in Table I. The as-grown IGZO films $[O_2/(Ar + O_2) = 2\%]$ are postannealed in air for 1 h at 300 °C, 600 °C, 700 °C, 800 °C, and 900 °C. The thickness of all films is set at 200 nm.

The crystal structures of the films is analyzed using x-ray diffraction [(XRD) XRD-6000, Shimadzu] with Cu *K*-$\alpha$ radiation at 40 kV and 30 mA. The resistivity, the Hall mobility, and the carrier density are measured at room temperature using the four-point probe method and Hall-effect measurement in the van der Pauw geometry (Bio-Rad HL5500PC and Toyo ResiTest8300). The transmittance and reflectance of the films are measured using an optical spectrophotometer (UV-3150, Shimadzu) in the spectral range of 190–2500 nm. Samples for transmission electron microscopy [(TEM) JEOL JEM 4010 at 400 kV] are

TABLE I. Electrical properties of amorphous IGZO films deposited under various sputtering ambients. Carrier density ($n_e$), Hall mobility ($\mu$), and resistivity ($R$) are given.

| Sample | Gas flow ratio | $n_e$ ($cm^{-3}$) | $\mu$ ($cm^2/V\,s$) | $R$ ($\Omega\,cm$) |
|---|---|---|---|---|
| *A* | Ar = 100% | $2.60 \times 10^{19}$ | 15.5 | 0.015 |
| *B* | $H_2/(Ar + H_2) = 5\%$ | $2.54 \times 10^{18}$ | 14.8 | 0.17 |
| *C* | $O_2/(Ar + O_2) = 1\%$ | $6.02 \times 10^{17}$ | 14.6 | 0.71 |
| As grown | $O_2/(Ar + O_2) = 2\%$ | $1.53 \times 10^{14}$ | 11.0 | $3.71 \times 10^3$ |

prepared using a mechanical thinning process followed by ion milling. We use a scanning electron microscope with a Schottky-emission-type gun (HITACHI S-4300SE) as the excitation source for the CL measurements. The CL signals are collected using an ellipsoidal mirror and optical fiber and detected using a Jobin Yvon HR-320 single monochromator equipped with a CCD. We record the CL spectra at an acceleration voltage of 3 kV with a beam current of less than 5 nA at 35 K. PALS measurements are performed using $^{22}$Na-based pulsed-positron-beam equipment (Fuji-Imvac, Japan), where the IGZO films are fabricated at Si wafers with a natural oxidation layer. The experiments are performed at room temperature in vacuum. The method involves implanting a film with positrons and detecting the 511-keV $\gamma$ quanta produced by the subsequent electron-positron annihilation. The implanting depth of the positrons is estimated to be 100 nm assuming a density of 6.0 $g/cm^3$ for the IGZO films [27]. The peak-to-background ratio is approximately $10^4$, and $5 \times 10^6$ counts of positron annihilation events are collected.

EXAFS measurements are conducted at beam lines BL06, BL07, and BL11 of the SAGA Light Source [34–36]. The EXAFS spectra of all IGZO films are obtained in the convergent electron yield mode, and the EXAFS spectra of the reference samples (standard crystalline $IGZO_4$ powders) are obtained in the transmission mode. All measurements are performed at room temperature. The EXAFS data are processed and analyzed using ATHENA and ARTEMIS codes [37]. After the $\chi(k)$ spectra are extracted by removing the background using the Cook and Sayers method, the magnitudes of the Fourier transforms are obtained in the range of $k = 3.0$–$11$ $Å^{-1}$ for the Ga $K$ edge, $k = 2.0$–$10$ $Å^{-1}$ for the Zn $K$ edge and the In $K$ edge with the $k^3$ weighting of a Hanning window to obtain radial distribution functions. The data are fitted in the $R$ space with a fit range of $R = 1.0$–$1.9$ Å for the Ga $K$ edge, $R = 1.1$–$1.9$ Å for the Zn $K$ edge, and $R = 1.2$–$2.1$ Å for the In $K$ edge to obtain the interatomic distance and the coordination number.

## III. RESULTS AND DISCUSSION

### A. Structural properties

XRD patterns show that the as grown IGZO films are amorphous, and the IGZO films maintain their amorphous state up to an annealing temperature of 600 °C in air. TEM observations show that a few nanocrystallites emerge in the surface of amorphous IGZO films postannealed at 600 °C. Above 600 °C, sharp XRD peaks are observed, indicating the crystallization of amorphous IGZO films, as reported in our previous study [28].

### B. Evolution of the local structure of metal-oxygen bonds following postannealing

In amorphous IGZO, the deep subgap states, as well as VB tails near the VBM, are attributed to the varied oxygen coordination numbers around metal atoms [16,22]. We use EXAFS measurements to investigate the changes in the oxygen coordination number around metal atoms with increasing postannealing temperature. Figures 1(a)–1(c) show the Fourier-transformed (FT) EXAFS spectra of the as-grown and postannealed IGZO films, as well as the standard $IGZO_4$ powder, as a function of the phase-uncorrected interatomic distance. For the crystalline $IGZO_4$ powder, all cation $K$-edge spectra show two obvious peaks,

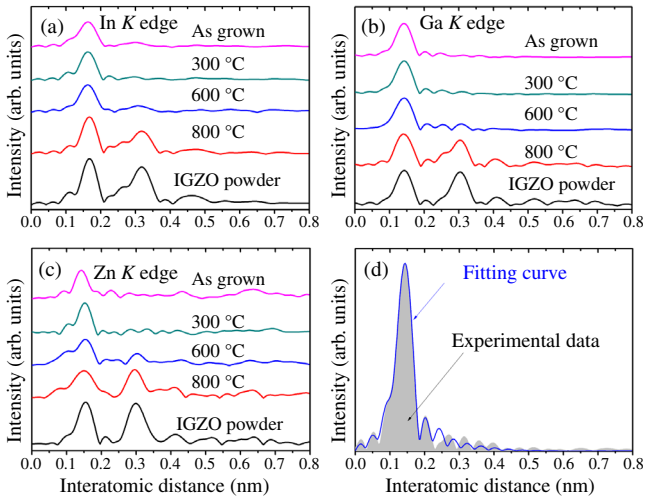


FIG. 1. Coordination structures in amorphous and postannealed IGZO thin films. (a)–(c) The measured FT EXAFS spectra without phase correction for the In $K$ edge, the Ga $K$ edge, and the Zn $K$ edge, respectively. (d) The measured FT EXAFS spectra (gray) are compared with the fit spectra to estimate the coordination number of the nearest oxygen and the interatomic distance between the cation and the oxygen, where the measured FT EXAFS spectra of the Ga $K$ edge without phase correction come from the as-grown IGZO film.

each of which corresponds to the nearest oxygen atom and the second-nearest cation. Only one peak from the nearest-neighbor oxygen is observed in the case of the as-grown IGZO film and the postannealed IGZO films at 300 °C and 600 °C, which indicates that medium-range ordering at distances equal to or longer than the second-neighbor distance is nearly lost around cations. By contrast, two main peaks are observed in the spectrum of the IGZO film postannealed at 800 °C, and these two peaks are similar to those observed in the spectrum of the crystalline $IGZO_4$ powder and indicate medium-range ordering in the IGZO films. As for long-range ordering, we demonstrated in previous studies that amorphous IGZO films are crystallized with the polycrystalline structure at 700 °C [28].

The crystal structure of $IGZO_4$ consists of $InO_6$ octahedron layers and $GaO(ZnO)^+$ layers, in which the $InO_6$ octahedron layers are connected two dimensionally in an edge-sharing network, and the Ga and Zn ions occupy the trigonal-bipyramidal sites in the $GaO(ZnO)^+$ layers in an $IGZO_4$ crystal [38,39]. To obtain the oxygen coordination number of amorphous or polycrystalline IGZO films, we first use the nearest-neighbor metal-oxygen coordination numbers in a theoretical crystal structure ($N_{In-O} = 6$, and $N_{Ga-O} = N_{Zn-O} = 5$) [38] to fit the EXAFS spectra of the crystalline IGZO powder to obtain the amplitude of the absorption spectra [37]. Then, we use the fixed amplitude to obtain the coordination numbers around metal atoms by fitting the EXAFS spectra of the as-grown and postannealed IGZO films [37]. Figure 1(d) shows that the fit of the first coordination shell agrees very well with the measured EXAFS spectra, where the first coordination shell is considered to be full of oxygen atoms around metal cations.

Table II lists the interatomic distances and the coordination numbers between the cations and the oxygen atoms. The averaged oxygen coordination numbers of each metal ion indicate that the clusters are near $InO_6$, $GaO_5$, and $ZnO_5$ in the amorphous structure. In the case of the as-grown IGZO film, the nearest-neighbor metal-oxygen coordination numbers are smaller than those of the crystalline IGZO powder, except in the case of the Ga—O bond. This finding implies that our as-grown IGZO films are in the non-stoichiometric state. With a postannealing temperature that increases from 300 °C to 800 °C, the coordination numbers of the In—O bond remain almost constant, and the coordination number of the Zn—O bond increases to values similar to those of the powder, which may be attributed to the reaction between oxygen from the postannealing ambient (air) and the amorphous IGZO films. By contrast, the coordination numbers of the Ga—O bond show a tendency to be larger than those of the crystalline $IGZO_4$ powder, suggesting the formation of oxygen-related defects (excess oxygen) in the local Ga—O structure. These results reveal the varied oxygen coordination numbers around the metal atoms during postannealing.

On the other hand, as the postannealing temperature increases, the metal-oxygen interatomic distances approach that of the crystalline $IGZO_4$ powder, possibly owing to structural relaxation during postannealing. For IGZO films postannealed at 800 °C, the In—O interatomic distance is 2.16 Å, which is approximately equal to that of the crystalline $IGZO_4$ powder and that listed in the crystallographic data of $IGZO_4$ crystals [40]. For the postannealed IGZO films, the Zn—O and Ga—O interatomic distances are almost kept at 1.97 and 1.88 Å, respectively, and are different from the values obtained by XRD precise measurements, in which an $IGZO_4$ single crystal is synthesized under high pressure [40]. This difference is the case because the fitted interatomic distances are the average values of all metal-oxygen interatomic distances in the first shell without considering the spatial configurations of the Zn(Ga)—O bonds in crystalline $IGZO_4$. In the $IGZO_4$ crystal, there exist three Zn(Ga)—O bonds (1.93 Å) between the central Zn (Ga) ion and the three oxygen ions at the corners of the basal triangle of the bipyramid, and two bonds between the Zn (Ga) and O ions at the top of the pyramid of the $InO_2$-layer side (1.98 Å) and that of the $GaZnO_2$-layer side (2.32 Å) [40]. Thus, the theoretical average interatomic distance of the Zn(Ga)—O bond is 2.02 Å in the $IGZO_4$ crystal. The fitted Zn-O interatomic distance (1.97 Å) is close to the theoretical average value, but the fitted Ga—O interatomic distance (1.88 Å) is considerably smaller than the theoretical average value. Regarding the nature of the chemical bond, where the Ga—O bond is stronger than the Zn—O bond [41], the interatomic distances of Ga—O and Zn—O should differ.

TABLE II. Local structural parameters of IGZO films evaluated by the first shell EXAFS fittings. For comparison, the EXAFS spectra of crystalline $IGZO_4$ (*c*-IGZO) powder are fitted using the same approach. Here, $N$ is the coordination number, $r$ is the phase-corrected interatomic distance between the cation and the oxygen, and $\sigma$ is the Debye-Waller factor.

| | In—O | | | Ga—O | | | Zn—O | | |
|---|---|---|---|---|---|---|---|---|---|
| Sample | $N$ | $r$ (Å) | $\sigma^2$ (Å$^2$) | $N$ | $r$ (Å) | $\sigma^2$ (Å$^2$) | $N$ | $r$ (Å) | $\sigma^2$ (Å$^2$) |
| As grown | 4.9(1.8) | 2.16(2) | 0.004 | 5.0(0.9) | 1.87(1) | 0.006 | 4.5(1.8) | 1.97(3) | 0.006 |
| 300 °C | 4.3(1.2) | 2.13(2) | 0.006 | 5.1(0.8) | 1.87(1) | 0.006 | 4.6(2.1) | 1.97(4) | 0.006 |
| 600 °C | 5.5(1.0) | 2.14(2) | 0.009 | 5.5(1.7) | 1.87(2) | 0.008 | 4.6(2.4) | 1.97(4) | 0.006 |
| 800 °C | 5.0(1.8) | 2.16(2) | 0.004 | 5.6(3.4) | 1.88(4) | 0.007 | 5.0(2.0) | 1.97(3) | 0.005 |
| *c*-IGZO powder | 6 (fixed) | 2.17(3) | 0.003 | 5 (fixed) | 1.87(2) | 0.005 | 5 (fixed) | 1.98(2) | 0.005 |

On the basis of the results of the relaxation calculations obtained by Orita *et al.* [42] for the $IGZO_4$ structure considering the strength of the metal-oxygen bond, the average Ga—O interatomic distance is 1.95 Å, and it is close to the fitted Ga—O interatomic distance in this paper. In fact, the same Ga—O bond distance (1.88 Å) have also been reported in other EXAFS measurements of IGZO films at SPring-8 [43]. Therefore, the deviation from the XRD precise measurement [40] may be ascribed to the method of sample fabrication. The interatomic distance of 1.88 Å is longer than that of the fourfold-coordination tetrahedral structure of $\beta$-$Ga_2O_3$ (1.83 Å) [44], indicating that the Ga ions possibly occupy fivefold-coordination sites.

### C. Formation of vacancy clusters following postannealing

PALS is a well-established technique for studying open volumes in materials directly at the atomic level, thus facilitating complete characterization of vacancy-type defect structures. The PALS spectra of the as-grown and postannealed IGZO films are shown in Fig. 2. For the as-grown IGZO films, curve ranges of 0 to approximately 2000 ps can be fitted well to a single line. The features of the PALS spectrum of the IGZO film postannealed at 300 °C are very similar to those of the spectrum of the as-grown IGZO films, but a slight increase in spectral intensity is observed from about 1500 ps in the case of the former. For postannealing temperatures higher than 300 °C, the intensity of the PALS spectrum in the long-lifetime region (from approximately 500 ps) increases in an obvious manner with an increasing postannealing temperature, suggesting that the PALS spectrum can be decomposed into two lifetime components, the short positron lifetime $\tau_1$ and the long positron lifetime $\tau_2$. It is worth noting that, although the PALS spectra of the as-grown IGZO film can be fit well using one lifetime component, the fit average lifetime (280 ps) is obviously longer than those $\tau_1$ values in other amorphous IGZO films postannealed at 300 °C and 600 °C, suggesting that the decomposition for the PALS spectra of the as-grown IGZO film is necessary [45].

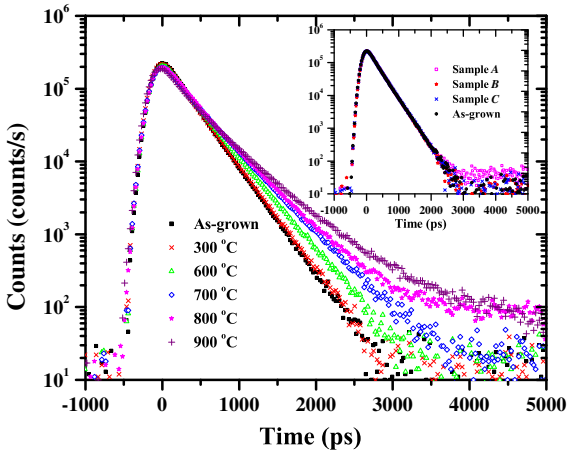


FIG. 2. PALS spectra of the as-grown IGZO film and postannealed IGZO films at different temperatures. (Inset) The PALS spectrum of amorphous IGZO films deposited under different sputtering conditions, which is summarized in Table I.

Table III shows the fit results of $\tau_1$ and $\tau_2$. The $\tau_1$ value is about 200 ps in the amorphous as-grown IGZO film and postannealed IGZO films at 300 °C and 600 °C, and it changes to 220–260 ps in the polycrystalline IGZO films postannealed above 600 °C. This larger $\tau_1$ in polycrystalline IGZO films than one in amorphous IGZO films is different from those observed in silicon material [46], in which $\tau_1$ is much longer in the amorphous state. The difference is due to the fact that the increase in $\tau_2$ is very large together with the strong intensity $I_2$ with an increasing postannealing temperature, resulting in a large $\tau_1$ value. So is the large uncertainty in $\tau_1$ of the polycrystalline IGZO films at different postannealing temperature in Table III. The fitted lifetime $\tau_1$ is considered to correspond to the positron lifetime in the IGZO structure. $\tau_1$ in the IGZO films is longer than those typical positron lifetimes in $In_2O_3$ films (183 ps) [47], $Ga_2O_3$ films (176 ps) [48], ZnO films (170 ps) [49], $SnO_2$ (175 ns) [50], and GaN films (156 ps) [51], which show free positron lifetimes in the lattice spacing.

The high values of $\tau_2$ in Table III suggest that annihilation mainly occurs in open-volume defects, which act as trapping centers for the positrons in the IGZO films, and the high-intensity $I_2$ of $\tau_2$ implies the near-saturation trapping of the positrons. When increasing the postannealing temperature to 600 °C, an increase in both $\tau_2$ and $I_2$ suggests an increase in both the size and the concentration of the open-volume defects. By contrast, an increase in $\tau_2$ together with a decrease in $I_2$ suggests an increase in the size of the open-volume defects. The lifetime of trapped positrons $\tau_2$ depends on the chemical environment and physical size of the open-volume defects [52]. The open-volume defects may possibly be attributed to (1) voids (> 1 nm in size), (2) dislocations, and (3) point defects. Discussions about the influence of these possible open volumes on positron trapping are given in the following.

(1) Voids. TEM observations are performed to observe the existence of voids in the as-grown

TABLE III. The short positron lifetime ($\tau_1$) and long positron lifetime ($\tau_2$) obtained by fitting the PALS spectra of the as-grown IGZO film and postannealed IGZO films. $I_1$ and $I_2$ are the relative intensities of $\tau_1$ and $\tau_2$, respectively.

| Sample | $\tau_1$ (ps) | $I_1$ (%) | $\tau_2$ (ps) | $I_2$ (%) |
|---|---|---|---|---|
| As grown | 202 | 23.2 | 303 | 76.8 |
| 300 °C | 188 | 17.6 | 310 | 82.4 |
| 600 °C | 197 | 17.8 | 349 | 82.2 |
| 700 °C | 223 | 27.1 | 403 | 72.9 |
| 800 °C | 256 | 46.5 | 456 | 53.5 |
| 900 °C | 264 | 53.2 | 540 | 46.8 |

and postannealed IGZO films. No voids or pores are observed, which is different from the observations in the case of the In-Sn-Zn oxide films [53]. Figure 3 shows the typical plane-view TEM images of the polycrystalline IGZO films, which is postannealed at 800 °C, and no voids are observed. Moreover, as indirect evidence, no void formation in the annealed IGZO films can be demonstrated based on the change in film density with increasing postannealing temperature. In the case of the void formation in postannealed IGZO films, the obvious increase in $\tau_2$ with an increasing postannealing temperature indicates that the void sizes and concentrations increase with an increasing postannealing temperature, and, consequently, the film density decreases. This prediction about the decreasing density with an increasing postannealing temperature is inconsistent with reported experimental observations [27,28], according to which the postannealing produced a much denser IGZO film. Therefore, the voids are not considered to exist in the present as-grown and postannealed films, and the increase in $\tau_2$ with an increasing postannealing temperature is not attributed to void formation.

(2) Dislocations. Figure 3(a) shows the existence of dislocations in the polycrystalline IGZO films postannealed at 800 °C. Around the dislocations, there exists a local lattice distortion, which is thought to produce an open volume. Do the dislocations affect the long-lifetime $\tau_2$ of positron trapping? In the PALS features, the intensity of the PALS spectra tends to increase in the long-lifetime region, as shown in Fig. 2, even in amorphous states, such as IGZO films postannealed at 300 °C and 500 °C (see Fig. S1 in the Supplemental Material [54]). However, no dislocations can be seen in the case of the IGZO films postannealed at 600 °C, where most of the film maintains the amorphous state and a few nanocrystallites without dislocations are observed in the film surface [27,28], and the amorphous IGZO films postannealed at 300 °C and 500 °C (see the Supplemental Material [54]) are believed to have no dislocations owing to structural relaxation. Thus, the increase in $\tau_2$ with increasing postannealing temperature cannot be associated with the formation of dislocation. In addition, although we observe stacking faults, as shown in Fig. 3(a), the stacking faults are not considered to produce the open-volume defects to trap positrons.

(3) Point defects. In the high-resolution TEM images shown in Fig. 3(b), the absence of Ga or Zn atoms along the Ga/Zn column can be clearly observed by comparison with the simulated atomic arrangement of the $IGZO_4$ structure, where the surrounding oxygen atoms around the Ga or Zn atoms may also miss because of the large space between the two metal atoms. Vacancy-type defects are considered to be produced easily in the amorphous structure, although they are invisible to conventional TEM. Here, vacancy-type defects are regarded as a cation- and/or oxygen-deficient defect formed by simply removing a host cation and/or oxygen atoms, followed by lattice relaxations in the amorphous structure. Discussions about whether the cation-related vacancy defects can be efficiently detected by PALS follow.

As a well-established tool for investigating point defects in condensed materials, PALS has been employed extensively to characterize vacancy-type defects as well [45]. Identification of the nature of the detected vacancy-type defects is complicated because we must consider the possibility of various charge states of the defects in IGZO films. Generally, the charge state (neutral, positively charged, or negatively charged) of the defect determines whether or not it can be efficiently detected by PALS [55]. Positively charged defects have the lowest probability for positron annihilation as a result of the long-range, repulsive Coulomb interaction between the positive charge and the positron [55]. Hence, positively charged vacancies such as positively ionized vacancy ($V_O^{2+}$ or $In^+$) [13,20] in IGZO films are considered much less likely to trap positrons. We confirm this conclusion by measuring the PALS spectra for IGZO films with different carrier densities, where the origin of carrier electrons in amorphous IGZO films is attributed

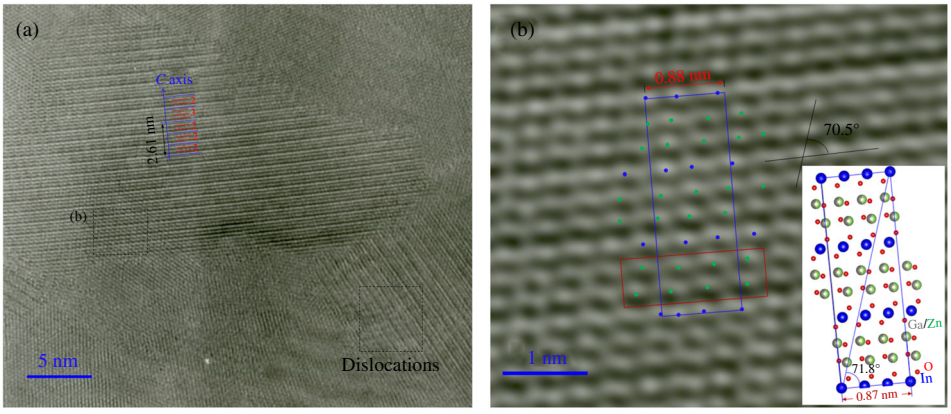


FIG. 3. (a) Plane-view TEM images of the IGZO film postannealed at 800 °C. The dashed rectangles show the vacancy clusters and dislocations. (b) High-resolution TEM image, which was created using fast Fourier transform and the following inverse fast Fourier transform of the dashed rectangle (b) in (a). The cation vacancies along the Ga/Zn column is highlighted by the red rectangle. The inset in (b) shows the simulated atomic model of the crystalline $IGZO_4$.

to the doubly positively charged oxygen vacancies ($V_O^{2+}$) [56]. As shown in the inset of Fig. 2, no obvious differences are observed in PALS spectra featuring IGZO films with different carrier densities (samples *A*–*C* and as-grown IGZO films), and this spectra feature suggests that $\tau_2$ should not be attributed to positively charged defects such as $V_O^{2+}$. Thus, the neutral or negatively charged vacancy or vacancy clusters are considered to trap positrons [13]. As for the neutral or negatively charged defects, small anion vacancies such as $V_O^0$ and $V_O^{2-}$, even if clustered together, have been reported to not trap positrons in such strongly cation-anion radius-mismatched compounds ($In_2O_3$ and InN) [48,57]. Hence, neutral or negatively charged cation vacancies ($V_M$), such as $V_{In}$, $V_{Ga}$ or $V_{Zn}$, are considered to be related to the defects detected with positrons. This inference is consistent with the high-resolution TEM observations, in which the absence of the cations is observed. On the basis of these results, the long-lifetime component $\tau_2$ is considered to be related to the $V_M$-related defects in the postannealed IGZO films.

Let us estimate the size of the $V_M$-related defects in the as-grown and postannealed IGZO films. For oxide semiconductor materials such as $In_2O_3$ and ZnO [48,49], the cation-vacancy lifetimes in such crystals are higher than the lifetime $\tau_1$ in bulk, usually by 40–80 ps. By contrast, $\tau_2$ is considerably larger than $\tau_1$, by about 150–250 ps, in the postannealed IGZO films. This large $\tau_2$ in the postannealed IGZO films implies that the $V_M$-related defects detected with positrons are most probably vacancy clusters involving both $V_M$ and $V_O$, such as those in $In_2O_3$ [48], $SnO_2$ [50], and ZnO [58,59]. It is thus suggested that $\tau_2$ is related to the formation of $V_M$-related vacancy clusters, which tend to form increasingly with an increasing postannealing temperature. In physics, $V_M$-related vacancy clusters can be understood as the absence of the cation together with the surrounding oxygen in amorphous or polycrystalline IGZO structures, which is charge neutral or negatively charged.

### D. Evolution of subgap states during postannealing

CL measurements are performed to examine the emission behaviors of the IGZO films with an increasing postannealing temperature. Figure 4(a) shows the CL spectra of the series of samples postannealed in air compared with the spectrum of the initial as-grown IGZO films, and Fig. 4(b) shows the CL spectra of the amorphous IGZO films deposited at different sputtering ambients. The intensities of all CL spectra are normalized to the peak maximum. The spectral features of the as-grown IGZO films and postannealed films at 300 °C and 600 °C are qualitatively similar, and a slight shift toward the short wavelength is observed with an increasing postannealing temperature. When the postannealing temperature is higher than 600 °C, the peak maximum of the emission bands quickly shifts from approximately 680 to about 580 nm, and the spectra show obvious asymmetry. To further

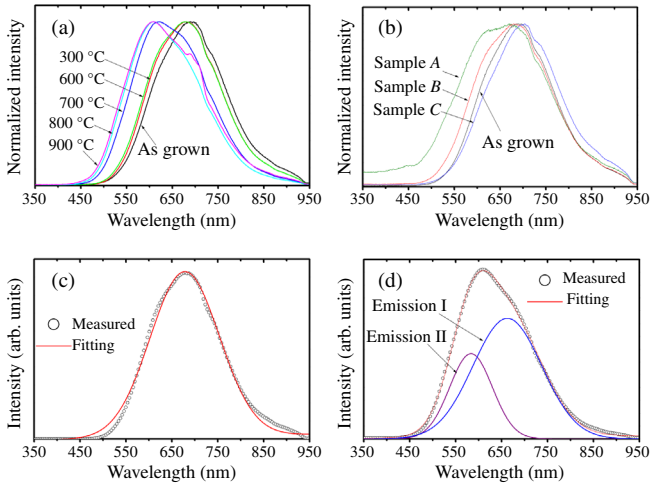


FIG. 4. (a) CL spectra of as-grown and postannealed IGZO films at different temperatures. (b) CL spectra of amorphous IGZO films deposited in different sputtering ambients compared with the as-grown IGZO films. Note that the intensities of all of the CL spectra are normalized to the peak maximum. (c),(d) Gaussian deconvolutions of the CL spectra. All of the CL measurements are performed at 35 K.

understand this asymmetric emission band, Gaussian deconvolutions of the spectra are performed into two bands centered at approximately 680 nm (1.85 eV) and about 580 nm (2.15 eV) [60], and the positions of these bands changes slightly at different postannealing temperatures. Figures 4(c) and 4(d) show that the fitted curves reproduce the CL spectra well.

Table IV lists the fitting results of the CL spectra. The positions of the two emission bands shift slightly toward the short wavelength as the postannealing temperature increases. Above 600 °C, the intensity ratio of the emission band at 1.85 eV to that at 2.15 eV is 0.5 to 0.7, indicating that the main luminescence still originates from the emission band at 1.85 eV. A similar emission band at 1.85 eV is reported in the photoluminescence spectra of amorphous IGZO films [61], and its position remains almost constant for various amorphous IGZO films deposited in different sputtering ambients, as shown in Fig. 4(b).

CL testing involves electron-radiation-induced excitation of an electron from the ground state to an excited state, and luminescence is the resultant spontaneous emission of light corresponding to the radiative transition when an electron drops from an upper to a lower energy level of either an intrinsic band state or an impurity level [62,63]. Because the emission bands are obviously smaller than the band gap of the IGZO films, as can inferred from Table IV, the intrinsic emission from the direct band-band transition is neglected. In Fig. 5, the extrinsic luminescence arising from the impurity levels in the forbidden energy gap of IGZO is summarized in terms of three general models: (1) relaxation of deep donors to the VB and to subsequent photon emission (type I); (2) radiative transition from the

TABLE IV. Results of the peak deconvolution of the CL spectra of as-grown and postannealed IGZO samples. CE is the center energy of the deconvoluted peak. $I_2/I_1$ is the intensity ratio of emission II to emission I. The optical band gap ($E_{opt}$) is also listed (estimated as the Tauc gap; see the absorption spectra of IGZO samples in Fig. S2 in the Supplemental Material [54]).

| | Emission I | | Emission II | | | |
|---|---|---|---|---|---|---|
| Sample | CE (nm) | FWHM (nm) | CE (nm) | FWHM (nm) | $I_2/I_1$ | $E_{opt}$ (eV) |
| As-depo. | 688 | 180 | ··· | ··· | 0.0 | 3.30 |
| 300 °C | 678 | 177 | ··· | ··· | 0.0 | 3.43 |
| 600 °C | 676 | 181 | ··· | ··· | 0.0 | 3.40 |
| 700 °C | 668 | 177 | 591 | 106 | 0.5 | 3.50 |
| 800 °C | 663 | 176 | 583 | 109 | 0.7 | 3.51 |
| 900 °C | 660 | 182 | 576 | 103 | 0.6 | 3.53 |

CB to the acceptor level, resulting in emission of a photon (type II); and (3) recombination between the donor and the acceptor (type III), which is called the donor-acceptor pair (DAP) recombination. The photon energy of a DAP recombination event is $E_{DA} = E_g - (E_D + E_A) + e^2/\epsilon R$, where $E_D$ and $E_A$ are the binding energies of the donor and the acceptor, respectively; $e$ the element charge; $\epsilon$ the dielectric constant; and $R$ is the donor-acceptor separation. Larger values of $R$ broaden the emission spectrum with less probability of radiative tunneling [63]. DAP recombination events have been found in other wide-band-gap oxide semiconductors such as ZnO and $In_2O_3$ [59,64].

Usually, the deep donors in $n$-type materials do not contribute to the luminescence in wide-band-gap semiconductors [65]. Herein, we assign the CL emission bands (1.85 and 2.15 eV) to the recombination between the CB electrons and/or the shallow donors near the CBM and the acceptors trapped in the band gap. In a case involving recombination between the CB electrons and the acceptors, the acceptor level is estimated to be located at approximately 1.2 eV above the VBM for an emission band at 1.85 eV, and about 0.95 eV above the VBM for an emission band at 2.15 eV, which is considered as the deep subgap state. These results are consistent with the experimental observation that the subgap states extend to 1.70 eV above the VBM from a HXPES measurement [21]. By contrast, the shallow donor levels are believed to exist near the CB in IGZO films, at least in the case of the as-grown IGZO films, because the as-grown IGZO films have the carrier densities of about $2.0 \times 10^{14}$ $cm^{-3}$, as summarized in Table I. In fact, in HXPES studies, the peak-shape subgap states near the CBM have been observed in the as-grown and postannealed IGZO films at postannealing temperatures of up to 800 °C, including the IGZO films deposited under a high oxygen flow ratio (3%) [31], which is similar to the sputtering condition in this paper. The donor level is estimated to be 0.1–0.3 eV below the CBM for amorphous IGZO films with carrier densities of approximately $10^{16}$ $cm^{-3}$ [66]. Thus, a DAP recombination involving shallow (delocalized) donors would lead to very small shifts from the viewpoint of the determination of the acceptor level.

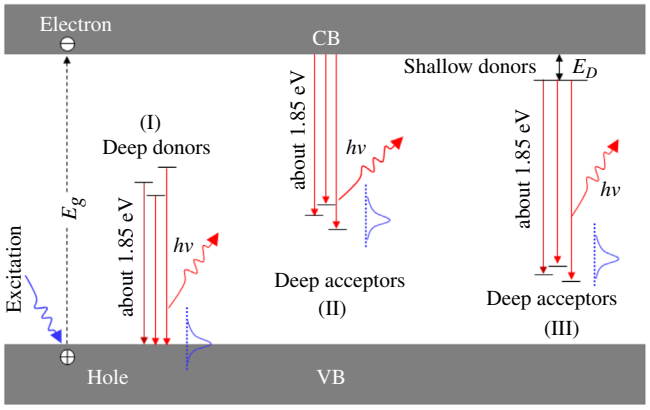


FIG. 5. Schematic illustration of possible cathodoluminescence mechanisms due to recombination processes in as-grown and postannealed IGZO films. CB, conduction band; VB, valence band; $E_g$, band gap; $E_D$, shallow donor level near the CBM. The main emission band at 1.85 eV and $E_g$ are marked to serve as a visual guide for understanding the defect energy levels.

On the other hand, an emission band at 2.15 eV is observed only in the cases with postannealed IGZO films above 600 °C. This emission band is possibly attributed to an increase in the band gap owing to structural relaxation during crystallization [27] because the energy difference between two fitted emission bands is about 0.24 eV for postannealed IGZO films above 600 °C, which is very close to the increase in the band gap (approximately 0.20 eV) from amorphous IGZO (as grown) to polycrystalline IGZO films postannealed at 700 °C, as listed in Table IV. It is worth noting that the postannealed IGZO films above 600 °C are composites for amorphous and crystalline phases. Although the crystallization temperature of amorphous IGZO is between 600 °C and 700 °C, the crystalline volume fraction in the postannealed IGZO film remain at 50% up to 900 °C [27]. Thus, the emission band at 2.15 eV may have originated from the polycrystalline region in the postannealed IGZO films, which has a larger band gap than that of the amorphous IGZO film [27].

Accurate determination of the microscopic physical origin of the CL emission bands (1.85 and 2.15 eV), including the defect type, needs to be combined with theoretical calculations and different experimental approaches, which is discussed below.

### E. Discussions

The next question concerns the microscopic nature of those defect levels as revealed by CL measurements, which could be due to the native defects or impurities or, alternatively, to extended defects such as the dislocations or grains shown in Fig. 3. The fact that the emission at

1.85 eV is present in the amorphous IGZO films (as-grown IGZO film and postannealed IGZO films at 300 °C and 600 °C), which have no extended defects, suggests that the extended defects themselves are not the origin of the emission at 1.85 eV. Therefore, we focus on point defects.

EXAFS measurements show the varied oxygen coordination numbers around the metal atoms during postannealing. With an increasing postannealing temperature, the Ga-O coordination number shows an increasing tendency to become larger than that of the crystalline $IGZO_4$ powder, indicating the formation of excess oxygen around Ga due to postannealing. By contrast, the coordination number of In-O remains almost constant and less than the stoichiometric value, and that of Zn—O increases toward the stoichiometric value, suggesting the existence of oxygen deficiency around the In and Zn atoms in the as-grown and postannealed IGZO films. These experimental results can be explained easily; that is, because the Ga—O bond is the strongest among the metal-oxygen bonds in the IGZO films [41], excess oxygens form easily around the Ga atoms, and formation of the oxygen deficiency surrounding the In and Zn atoms costs less energy than the formation of the oxygen deficiency around the Ga atoms. On the other hand, PALS results suggest that the $V_M$-related clusters are formed in the postannealed IGZO films with an increasing postannealing temperature. Note that defect structures detected using EXAFS and PALS measurements differ, in principle, where EXAFS is used to measure the $K$-edge adsorption spectra of cation elements and PALS is used to detect the cation-vacancy-related cluster. In the following, we discuss the energy levels of these defects and defect clusters based on first-principle calculations, and try to explain the defect levels revealed by CL from the evolution behavior following the postannealing of IGZO films.

The excess oxygen around the Ga atom is often considered the interstitial oxygen ($O_i$) in first-principle calculations [26,39]. Omura *et al.* calculated the electronic structure of two different $O_i$ configurations, namely, split oxygen [$O_i$ (split)] and octahedral oxygen [$O_i$ (oct)], in crystalline $IGZO_4$ [39]. $O_i$ (split) occupies a split interstitial site, forming a chemical bond with the host oxygen, which is similar to the oxygen molecule, whereas $O_i$ (oct) is located at an octahedral site coordinated by six oxygen atoms. The calculation results suggest that $O_i$ (split) is electrically inactive for electrons but works as the donor, and $O_i$ (oct) is electrically active and acts as the acceptor near the VB edge. On the other hand, in amorphous IGZO, Han *et al.* found that the most stable $O_i$ configuration in the neutral state is an O—O dimer between $O_i$ and the host oxygen, similar to the $O_i$ (split) case mentioned above [26]. This O—O dimer bond is broken easily by capturing two electrons, suggesting that $O_i$ acts as an acceptor, and the subsequent negatively charged level lies in the valence-band tail when additional Ga—O bonds form around the broken dimer compared with Zn—O bonds [26]. In terms of the acceptors, the acceptor level revealed by CL may be associated with these O—O dimers in amorphous IGZO and $O_i$ (oct) in crystalline IGZO. Another defect model related to excess oxygen called weakly bonded oxygen is reported experimentally by Ide *et al.* [67], and its level is located at approximately 2.3 eV below the CBM and close to the emission band at 2.15 eV in the present CL spectra. However, the weakly bonded oxygen is found in the IGZO films postannealed in an $O_3$ ambient, which has a stronger oxidization ability than $O_2$, or observed in those IGZO films postannealed in a high-quality $O_2$ ambient [32,67]. Moreover, Ide *et al.* [67] reported that $O_3$ postannealing at 300 °C caused serious deterioration, resulting in a large subthreshold swing and a large threshold value, but our IGZO-based TFTs postannealed even at 800 °C still deliver a good TFT performance [28]. Thus, such weakly bonded oxygen is considered different from the physical origin of present deep subgap states.

Oxygen-deficiency-related defects are observed around In and Zn atoms in the as-grown and postannealed IGZO films. In crystalline $IGZO_4$, oxygen vacancies form the deep-donor lever and do not create the free carriers [39], similar to other oxide semiconductors such as ZnO and $SnO_2$ [68,69]. By contrast, in the amorphous IGZO, several models of oxygen deficiency have been proposed to understand the electronic structure above the VBM [13,22,23]. Kamiya *et al.* found that the oxygen deficiencies form a shallow donor state near the CBM and a deep localized state at 0.4 to 1 eV above the VBM, depending on local atomic configurations [23]. Körner *et al.* suggested that the deep subgap states above the VBM can be attributed to the undercoordinated oxygen atoms in the amorphous network, where the undercoordinated oxygen is similar to the concept of the oxygen deficiencies [22]. Furthermore, Noh *et al.* showed that most oxygen deficiencies ($V_O$) above the VBM act as deep donors in amorphous IGZO, and the ionization of neutral $V_O$ by hole capture occurs more easily in amorphous IGZO than in crystalline IGZO [13]. These $V_O$ defect levels are located near the midgap. In both amorphous IGZO and crystalline IGZO, the oxygen deficiencies are suggested to act as electron donors, rather than acceptors. Therefore, the deep acceptors revealed by CL should not give rise to oxygen deficiency in the as-grown and postannealed IGZO films.

The $V_M$-related cluster may act as the acceptor because the possible negative charge makes it become trap electrons. To the best of our knowledge, so far, no theoretical calculations have been performed to study their electronic structure in amorphous and crystalline IGZO. However, first-principle calculations have been performed to study the formation energy of various cation vacancies in amorphous IGZO [70]. Compared with the formation energy of an oxygen vacancy (2.0 eV), the formation energy of a Zn vacancy is 4.1 eV, that of an In vacancy is 6.1 eV, and that of a Ga vacancy is 5.1 eV. Among these

cation vacancies, Zn vacancies have the lowest formation energy, and they may act as acceptors in amorphous or polycrystalline IGZO films, as those reported in ZnO [71]. Cluster formation may further decrease the formation energy. In addition, to some extent, the $V_M$-related clusters can be simplified and treated as excess oxygen in the amorphous structure, where the missing cation causes the surrounding oxygen to relax toward the surrounding cations. Under such an approximation, the excess oxygen may be considered the same as the $O_i$ discussed above. As a future extension of this work, it would be interesting to construct an atomic model of the $V_M$-related cluster and check to see whether a subsequent relaxation of the amorphous model systems leads to these observed subgap states in the CL spectra.

Combining our experimental observations with the theoretical calculation above, the deep acceptor level located at 1.85 or 2.15 below the CBM should be associated with the excess oxygen around the metal atoms, which may exist as the O—O dimer in the amorphous structure or as $O_i$ (oct) in the crystalline structure, as opposed to existing as an oxygen deficiency. There remains the possibility from the $V_M$-related clusters to form such the acceptor level in amorphous and polycrystalline IGZO structure. On the other hand, the donor level near the CBM is considered to originate from the oxygen deficiency, as was proposed by Kamiya *et al.* [23] and Han *et al.* [26].

In addition to oxygen deficiency and excess oxygen, two other defect models have also been proposed to form the deep subgap states [72,73]. Orui *et al.* found impurity hydrogens existing as $OH^-$ chemical bonding states, which originate mainly from water molecules in the residual gas during sputtering, could form a deep subgap state near the middle of the band gap [73]. They found that the $OH^-$ impurity desorbs from the film as the postannealing temperature increases to more than 600 °C. This result is inconsistent with the present experimental observations based on CL measurements, according to which the band emission at 1.85 eV exists in the postannealed films above 600 °C. Bang *et al.* proposed another defect model, in which the $H^-$ impurities are incorporated and stabilized at the oxygen-vacancy sites during the preparation of amorphous IGZO thin films [72], and such defect complexes form a deep subgap state located 0.4 eV above the VBM, which is considerably lower than the value revealed by CL measurements (1.65–2.15 eV above the VBM).

Now let us discuss the influence of these defects on the NBIS or PBS instability in amorphous IGZO TFTs. NBIS instability has been reported to occur under illumination from a photon energy of approximately 2.3 eV, and the microscopic origin of this instability is assumed to be the formation of photoinduced holes owing to the existence of the deep subgap [9,17]. This photon energy is higher than the emission band of 1.85 eV in the CL spectra. However, in the case of DAP recombination, when the shallow donor level is located at 0.3 eV below the CBM [66], the acceptor level is located at about 2.15 eV below the CBM, which is close to 2.3 eV. Thus, the acceptor levels revealed by CL may be associated with the NBIS instability. As discussed on the physical origin of the NBIS instability above, the emission band at 1.85 eV is associated with the excess oxygen around the metal atoms, located at about 0.9 eV above the VBM, which may be ascribed to the O—O dimer in the amorphous IGZO, as proposed by Han *et al.* [26]. When a negative gate bias combined with light exposure is applied to amorphous IGZO TFTs, the negatively charged $O_i$ releases the electrons so that the $O_i$ defect can recover the stable O—O dimer configurations, and the released electrons induce a negative shift of the threshold value. On the other hand, the microscopic origin of the PBS instability is associated with the electron traps in bulk amorphous IGZO [26], and the positive shift of the threshold value can be explained by the negative charge of those acceptors. The calculation shows that the $O_i$ around Ga atoms acts as a double acceptor near the VBM [26] and hence contributes a net negative charge when the TFT is turned on [15]. In addition to $O_i$, a number of other point defects ought to be considered, such as a $V_M$-related cluster. According to first-principle calculations of amorphous IGZO [70], Zn vacancies have a lower formation energy than In and Ga vacancies, which may act as acceptors, as in ZnO [71], and give rise to the PBS instability. However, the number of possible point defects and/or defect complexes for $V_M$-related clusters in an amorphous network makes the task of identifying the defects responsible for PBS rather difficult.

## IV. CONCLUSIONS

In this paper, we investigate the evolution behavior of defect structures and subgap states in IGZO films with an increasing postannealing temperature. EXAFS measurements indicate the varied oxygen coordination numbers around metal atoms in the IGZO films during postannealing. Postannealing causes the metal-oxygen interatomic distances to approach the values of the crystalline IGZO powder. With an increasing postannealing temperature, the Ga—O coordination number shows a tendency to increase to values larger than that of the crystalline IGZO powder, indicating the formation of excess oxygen around Ga due to postannealing. By contrast, the coordination number of In-O remains almost constant and is less than the stoichiometric value, and the coordination number of Zn-O increases toward the stoichiometric value, suggesting the existence of an oxygen deficiency around In and Zn atoms in the as-grown and postannealed IGZO films. On the other hand, PALS measurements show an increase in the long-lifetime region of the PALS spectra with an increasing postannealing temperature, suggesting the existence of neutral or negatively charged $V_M$-related clusters in the as-grown and postannealed IGZO films. CL spectra

show a main emission band with a center energy of approximately 1.85 eV in the case of the as-grown and postannealed IGZO films, and a distinct shoulder located at about 2.15 eV in the case of IGZO films postannealed above 600 °C. These two emission bands are assigned to the recombination between the CB electrons and/or the shallow donors near the CBM and the acceptors trapped above the VBM. The shallow donors should originate from the oxygen deficiency, and the acceptors may originate from the interstitial oxygen or the $V_M$-related clusters. We expect that these findings will help to advance understanding of the instability of amorphous IGZO-based TFTs, especially environment-dependent instability.

## ACKNOWLEDGMENTS

J. Jia acknowledges the funding from JSPS KAKENHI Grant-in-Aid for Young Scientists (B) (Grant No. 16K21338). J. Jia, T. Okajiama, and Y. Shigesato acknowledge the funding from JSPS KAKENHI Grant-in-Aid for Scientific Research (C) (Grant No. 16K04966). XAFS spectra measurements using synchrotron radiation are performed at beam lines BL06, BL07, and BL11 of SAGA-LS (Proposal No. 1504023F). We also thank Masaaki Takeda at Toray Research Center for the discussions about the PALS spectra.

[1] X. Yu, T. J. Marks, and A. Facchetti, Metal oxides for optoelectronic applications, Nat. Mater. **15**, 383 (2016).
[2] K. Nomura, H. Ohta, A. Takagi, T. Kamiya, M. Hirano, and H. Hosono, Room-temperature fabrication of transparent flexible thin-film transistors using amorphous oxide semiconductors, Nature (London) **432**, 488 (2004).
[3] J. Jia, Y. Torigoshi, and Y. Shigesato, *In situ* analyses on negative ions in the indium-gallium-zinc oxide sputtering process, Appl. Phys. Lett. **103**, 013501 (2013).
[4] J. Jia, Y. Torigoshi, E. Kawashima, F. Utsuno, K. Yano, and Y. Shigesato, Amorphous indium-tin-zinc oxide films deposited by magnetron sputtering with various reactive gases: Spatial distribution of thin film transistor performance, Appl. Phys. Lett. **106**, 023502 (2015).
[5] J. H. Song, K. S. Kim, Y.G, Mo, R. Choi, and J. K. Keong, Achieving high field-effect mobility exceeding 50 $cm^2/V\,s$ in In-Zn-Sn-O thin-film transistors, IEEE Electron Device Lett. **35**, 853 (2014).
[6] J. K. Jeong, H. W. Yang, J. H. Jeong, Y.-G Mo, and H. D. Kim, Origin of threshold voltage instability in indium-gallium-zinc oxide thin film transistors, Appl. Phys. Lett. **93**, 123508 (2008).
[7] Y.-S Lee, E. K. -H Yu, D.-H Shim, H.-S Kong, L. Bie, and J. Kanicki, Oxygen flow effects on electrical properties, stability, and density of states of amorphous In-Ga-Zn-O thin-film transistors, Jpn. J. Appl. Phys. **53**, 121101 (2014).
[8] J. Jang, D. G. Kim, D. M. Kim, S.-J. Choi, J.-H. Lim, J.-H. Lee, Y.-S. Kim, B. D. Ahn, and D. H. Kim, Investigation on the negative bias illumination stress-induced instability of amorphous indium-tin-zinc-oxide thin film transistors, Appl. Phys. Lett. **105**, 152108 (2014).
[9] K. Takechi, M. Nakata, T. Eguchi, H. Yamaguchi, and S. Kaneko, Comparison of ultraviolet photo-field effects between hydrogenated amorphous silicon and amorphous $InGaZnO_4$ thin-film transistors, Jpn. J. Appl. Phys. **48**, 010203 (2009).
[10] P. Liu, Y. Chou, L. Teng, F. Li, and H. Shieh, Nitrogenated amorphous InGaZnO thin film transistor, Appl. Phys. Lett. **98**, 052102 (2011).
[11] J. Robertson and Y. Guo, Light induced instability mechanism in amorphous InGaZn oxide semiconductors, Appl. Phys. Lett. **104**, 162102 (2014).
[12] K. Nomura, T. Kamiya, H. Yanagi, E. Ikenaga, K. Yang, K. Kobayashi, M. Hirano, and H. Hosono, Subgap states in transparent amorphous oxide semiconductor, In-Ga-Zn-O, observed by bulk sensitive x-ray photoelectron spectroscopy, Appl. Phys. Lett. **92**, 202117 (2008).
[13] H. Noh, K. J. Chang, B. Ryu, and W. J. Lee, Electronic structure of oxygen-vacancy defects in amorphous In-Ga-Zn-O semiconductors, Phys. Rev. B **84**, 115205 (2011).
[14] J. Lee, J. Park, Y. S. Pyo, D. B. Lee, E. H. Kim, D. Styakhilev, T. W. Kim, D. U. Jin, and Y.-G Mo, The influence of the gate dielectrics on threshold voltage instability in amorphous indium-gallium-zinc oxide thin film transistors, Appl. Phys. Lett. **95**, 123502 (2009).
[15] M. D. H. Chowdhury, P. Migliorato, and J. Jang, Time-temperature dependence of positive gate bias stress and recovery in amorphous indium-gallium-zinc-oxide thin-film-transistors, Appl. Phys. Lett. **98**, 153511 (2011).
[16] W. H. Han and K. J. Chang, Subgap States near the Conduction-Band Edge due to Undercoordinated Cations in Amorphous In-Ga-Zn-O and Zn-Sn-O Semiconductors, Phys. Rev. Applied **6**, 044011 (2016).
[17] K. Nomura, T. Kamiya, and H. Hosono, Highly stable amorphous In-Ga-Zn-O thin-film transistors produced by eliminating deep subgap defects, Appl. Phys. Lett. **99**, 053505 (2011).
[18] S. Yang, K. H. Ji, U. K. Kim, C. S. Hwang, S. K. Park, C. Hwang, J. Jang, and J. K. Jeong, Suppression in the negative bias illumination instability of Zn-Sn-O transistor using oxygen plasma treatment, Appl. Phys. Lett. **99**, 102103 (2011).
[19] K.-H. Lee, J. S. Jung, K. S. Son, J. S. Park, T. S. Kim, R. Choi, J. K. Jeong, J.-Y. Kwon, B. Koo, and S. Lee, The effect of moisture on the photon-enhanced negative bias thermal instability in Ga-In-Zn-O thin film transistors, Appl. Phys. Lett. **95**, 232106 (2009).
[20] S. Sallis, N. F. Quarkenbush, D. S. Williams, M. Senger, J. C. Woicik, B. E. White, and L. F. J. Piper, Deep subgap feature in amorphous indium gallium zinc oxide: Evidence against reduced indium, Phys. Status Solidi A **212**, 1471 (2015).
[21] K. Nomura, T. Kamiya, E. Ikenaga, H. Yanagi, K. Kobayashi, and H. Hosono, Depth analysis of subgap electronic states in amorphous oxide semiconductor, *a*-In-Ga-Zn-O, studied by hard x-ray photoelectron spectroscopy, J. Appl. Phys. **109**, 073726 (2011).
[22] W. Körner, D. F. Urban, and C. Elsässer, Origin of subgap states in amorphous In-Ga-Zn-O, J. Appl. Phys. **114**, 163704 (2013).

[23] T. Kamiya, K. Nomura, and H. Hosono, Electronic structure of the amorphous oxide semiconductor $a$-$InGaZnO_{4-x}$: Tauc-Lorentz optical model and origins of subgap states, Phys. Status Solidi A **206**, 860 (2009).

[24] T. Kamiya, K. Nomura, M. Hirano, and H. Hosono, Electronic structure of oxygen deficient amorphous oxide semiconductor $a$-$InGaZnO_{4-x}$: Optical analyses and first-principle calculations, Phys. Status Solidi C **5**, 3098 (2008).

[25] T. Kamiya, K. Nomura, and H. Hosono, Subgap states, doping and defect formation energies in amorphous oxide semiconductor $a$-$InGaZnO_4$ studied by density functional theory, Phys. Status Solidi A **207**, 1698 (2010).

[26] W. H. Han, Y. J. Oh, K. J. Chang, and J. Park, Electronic Structure of Oxygen Interstitial Defects in Amorphous In-Ga-Zn-O Semiconductors and Implications for Device Behavior, Phys. Rev. Applied **3**, 044008 (2015).

[27] K. Ide, K. Nomura, H. Hiramatsu, T. Kamiya, and H. Hosono, Structural relaxation in amorphous oxide semiconductor, $a$-In-Ga-Zn-O, J. Appl. Phys. **111**, 073513 (2012).

[28] A. Suko, J. Jia, S. Nakamura, E. Kawashima, F. Utsuno, K. Yano, and Y. Shigesato, Crystallization behavior of amorphous indium-gallium-zinc-oxide films and its effects on thin-film transistor performance, Jpn. J. Appl. Phys. **55**, 035504 (2016).

[29] M. R. Moon, S. Na, H. Jeon, C.-H. An, K. Park, D. Jung, H. Kim, Y.-B. Lee, and H.-J. Lee, Effects of substrate heating on the amorphous structure of InGaZnO films and the electrical properties of their thin film transistors, Appl. Phys. Express **3**, 111101 (2010).

[30] S. Yoon, Y. J. Tak, D. H. Yoon, U. H. Choi, J. Park, B. D. Ahn, and H. J. Kim, Study of nitrogen high-pressure annealing on InGaZnO thin-film transistors, ACS Appl. Mater. Interfaces **6**, 13496 (2014).

[31] H. Tang, K. Ide, H. Hiramatsu, S. Ueda, N. Ohashi, H. Kumomi, H. Hosono, and T. Kamiya, Effects of thermal annealing on elimination of deep defects in amorphous In-Ga-Zn-O thin-film transistors, Thin Solid Films **614**, 73 (2016).

[32] K. Ide, Y. Kikuchi, K. Nomura, T. Kamiya, and H. Hosono, Effects of low-temperature ozone annealing on operation characteristics of amorphous In-Ga-Zn-O thin-film transistors, Thin Solid Films **520**, 3787 (2012).

[33] T. Yoshikawa, T. Yagi, N. Oka, J. Jia, Y. Yamashita, K. Hattori, Y. Seino, N. Taketoshi, T. Baba, and Y. Shigesato, Thermal conductivity of amorphous indium-gallium-zinc oxide thin films, Appl. Phys. Express **6**, 021101 (2013).

[34] S. Yoshioka, T. Ishioka, H. Okabe, A. Harata, Y. Soejima, K. Hara, and T. Okajima, Kyushu university beamline, BL06, at SAGA Light Source, Diamond Light Source Proc. **1**, e129 (2011).

[35] M. Kawamoto, K. Sumitani, and T. Okajima, The design of superconducting wiggler beamline BL7 at SAGA-LS, AIP Conf. Proc. **1234**, 355 (2010).

[36] T. Okajima, K. Sumitani, M. Kawamoto, and E. Kobayashi, X-ray absorption spectroscopy using BL11 at SAGA-LS, and its applications for materials science, J. Phys. Conf. Ser. **430**, 012088 (2013).

[37] B. Ravel and M. Newville, ATHENA, ARTEMIS, HEPHAESTUS: Data analysis for x-ray absorption spectroscopy using IFEFFIT, J. Synchrotron Radiat. **12**, 537 (2005).

[38] K. Nomura, T. Kamiya, H. Ohta, T. Uruga, M. Hirano, and H. Hosono, Local coordination structure and electronic structure of the large electron mobility amorphous oxide semiconductor In-Ga-Zn-O: Experiment and *ab initio* calculations, Phys. Rev. B **75**, 035212 (2007).

[39] H. Omura, H. Kumomi, K. Nomura, T. Kamiya, M. Hirano, and H. Hosono, First-principles study of native point defects in crystalline indium gallium zinc oxide, J. Appl. Phys. **105**, 093712 (2009).

[40] M. Nespolo, A. Sato, T. Osawa, and H. Ohashi, Synthesis, crystal structure and charge distribution of $InGaZnO_4$, X-ray diffraction study of 20 kb single crystal and 50 kb twin by reticular merohedry, Cryst. Res. Technol. **35**, 151 (2000).

[41] Y.-R. Luo, *Comprehensive Handbook of Chemical Bond Energies* (CRC Press, New York, 2007), p. 1080.

[42] M. Orita, H. Tanji, M. Mizuno, H. Adachi, and I. Tanaka, Mechanism of electrical conductivity of transparent $InGaZnO_4$, Phys. Rev. B **61**, 1811 (2000).

[43] H. Yabuta, N. Kaji, M. Shimada, T. Aiba, K. Takada, H. Omura, T. Mukaide, I. Hirosawa, T. Koganezawa, and H. Kumomi, Microscopic structure and electrical transport property of sputter-deposited amorphous indiumgallium-zinc oxide semiconductor films, J. Phys. Conf. Ser. **518**, 012001 (2014).

[44] S. Geller, Crystal structure of $\beta$-$Ga_2O_3$, J. Chem. Phys. **33**, 676 (1960).

[45] F. Tuomisto and I. Makkonen, Defect identification in semiconductors with positron annihilation: Experiment and theory, Rev. Mod. Phys. **85**, 1583 (2013).

[46] R. Krause-Rehberg and H. S. Leipner, *Positron Annihilation in Semiconductors: Defect Studies* (Springer, Berlin, 1999), p. 178.

[47] E. Korhonen, F. Tuomisto, D. Gogova, G. Wagner, M. Baldini, Z. Galazka, R. Schewski, and M. Albrecht, Electrical compensation by Ga vacancies in $Ga_2O_3$ thin films, Appl. Phys. Lett. **106**, 242103 (2015).

[48] E. Korhonen, F. Tuomisto, O. Bierwagen, J. S. Speck, and Z. Galazka, Compensating vacancy defects in Sn- and Mg-doped $In_2O_3$, Phys. Rev. B **90**, 245307 (2014).

[49] F. Tuomisto, V. Ranki, K. Saarinen, and D. C. Look, Evidence of the Zn Vacancy Acting as the Dominant Acceptor in $n$-Type ZnO, Phys. Rev. Lett. **91**, 205502 (2003).

[50] P. R. Guagliardo, E. R. Vance, Z. Zhang, J. Davis, J. F. Williams, and S. N. Samarin, Positron annihilation lifetime studies of Nb-doped $TiO_2$, $SnO_2$, and $ZrO_2$, J. Am. Ceram. Soc. **95**, 1727 (2012).

[51] K. Saarinen, T. Laine, S. Kuisma, J. Nissila, P. Hautojarvi, L. Dobrzynski, J. M. Baranowski, K. Pakula, R. Stepniewski, M. Wojdak, A. Wysmolek, T. Suski, M. Leszczynski, I. Grzegory, and S. Porowski, Observation of Native Ga Vacancies in GaN by Positron Annihilation, Phys. Rev. Lett. **79**, 3030 (1997).

[52] X. Yu, J. Smith, N. Zhou, L. Zeng, P. Guo, Y. Xia, A. Alvarez, S. Aghion, H. Lin, J. Yu, R. P. H. Chang, M. J. Bedzyk, R. Ferragut, T. J. Marks, and A. Facchetti, Spray-combustion synthesis: Efficient solution route to high-performance oxide transistors, Proc. Natl. Acad. Sci. U.S.A. **112**, 3217 (2015).

[53] J. Jia, Y. Torigoshi, A. Suko, S. Nakamura, E. Kawashima, F. Utsuno, and Y. Shigesato, Effect of nitrogen doping on

structural, electrical and optical properties in In-Sn-Zn oxide thin films, Appl. Surf. Sci. **396**, 897 (2017).

[54] See Supplemental Material at http://link.aps.org/supplemental/10.1103/PhysRevApplied.9.014018 for the PALS spectra at 500 ℃ (Fig. S1) and the aborption spectra of IGZO samples (Fig. S2).

[55] X. Hu, T. Koyanagi, Y. Katoh, and B. D. Wirth, Positron annihilation spectroscopy investigation of vacancy defects in neutron-irradiated 3*C*-SiC, Phys. Rev. B **95**, 104103 (2017).

[56] A. U. Adler, T. D. Yeh, D. B. Buchholz, R. P. H. Chang, and T. O. Mason, Quasi-reversible point defect relaxation in amorphous In-Ga-Zn-O thin films by *in situ* electrical measurements, Appl. Phys. Lett. **102**, 122103 (2013).

[57] C. Rauch, I. Makkonen, and F. Tuomisto, Identifying vacancy complexes in compound semiconductors with positron annihilation spectroscopy: A case study of InN, Phys. Rev. B **84**, 125201 (2011).

[58] R. Vidya, P. Ravindran, H. Fjellvag, B. G. Svensson, E. Monakhov, M. Ganchenkova, and R. M. Nieminen, Energetics of intrinsic defects and their complexes in ZnO investigated by density functional calculations, Phys. Rev. B **83**, 045206 (2011).

[59] M. Li, G. Xing, G. Xing, B. Wu, T. Wu, X. Zhang, and T. C. Sum, Origin of green emission and charge trapping dynamics in ZnO nanowires, Phys. Rev. B **87**, 115309 (2013).

[60] E. K. Yu, S. Jun, D. H. Kim, and J. Kanicki, Density of states of amorphous In-Ga-Zn-O from electrical and optical characterization, J. Appl. Phys. **116**, 154505 (2014).

[61] N. Yamaguchi, S. Taniguchi, T. Miyajima, and M. Ikeda, Optical and electrical properties of amorphous InGaZnO, J. Vac. Sci. Technol. B **27**, 1746 (2009).

[62] M. A. Reshchikov and H. Morkoc, Luminescence properties of defects in GaN, J. Appl. Phys. **97**, 061301 (2005).

[63] D. R. Vij and N. Singh, *Luminescence and Related Properties of II-VI Semiconductors* (Nova Science Publishers, Commack, NY, 1998).

[64] Z. P. Wei, D. L. Guo, B. Liu, R. Chen, L. M. Wong, W. F. Yang, S. J. Wang, H. D. Sun, and T. Wu, Ultraviolet light emission and excitonic fine structures in ultrathin single-crystalline indium oxide nanowires, Appl. Phys. Lett. **96**, 031902 (2010).

[65] M. A. Reshchikov and R. Y. Korotkov, Analysis of the temperature and excitation intensity dependencies of photoluminescence in undoped GaN films, Phys. Rev. B **64**, 115205 (2001).

[66] M. Kimura, T. Nakanishi, K. Nomura, T. Kamiya, and H. Hosono, Trap densities in amorphous-$InGaZnO_4$ thin-film transistors, Appl. Phys. Lett. **92**, 133512 (2008).

[67] K. Ide, Y. Kikuchi, K. Nomura, M. Kimura, T. Kamiya, and H. Hosono, Effects of excess oxygen on operation characteristics of amorphous In-Ga-Zn-O thin-film transistors, Appl. Phys. Lett. **99**, 093507 (2011).

[68] S. Lany and A. Zunger, Dopability, Intrinsic Conductivity, and Nonstoichiometry of Transparent Conducting Oxides, Phys. Rev. Lett. **98**, 045501 (2007).

[69] K. Singh, A. Janotti, M. Scheffler, and C. G. Van de Walle, Sources of Electrical Conductivity in $SnO_2$, Phys. Rev. Lett. **101**, 055502 (2008).

[70] T. Kamiya, K. Nomura, and H. Hosono, Present status of amorphous In-Ga-Zn-O thin-film transistors, Sci. Technol. Adv. Mater. **11**, 044305 (2010).

[71] S. J. Clark, J. Roberston, S. Lany, and A. Zunger, Intrinsic defects in ZnO calculated by screened exchange and hybrid density functionals, Phys. Rev. B **81**, 115311 (2010).

[72] J. Bang, S. Matsuishi, and H. Hosono, Hydrogen anion and subgap states in amorphous In-Ga-Zn-O thin films for TFT applications, Appl. Phys. Lett. **110**, 232105 (2017).

[73] T. Orui, J. Herms, Y. Hanyu, S. Ueda, K. Watanabe, I. Sakaguchi, N. Ohashi, H. Hiramatsu, H. Kumomi, H. Hosono, and T. Kamiya, Charge compensation by excess oxygen in amorphous In-Ga-Zn-O films deposited by pulsed laser deposition, J. Disp. Technol. **11**, 518 (2015).